

Perturbation of Microfluidic Transport Following Electrokinetic Injection through a Nanocapillary Array Membrane: Injection and Biphasic Recovery

Enid N. Gatimu,[†] Xiaozhong Jin,[‡] Narayan Aluru,[‡] and Paul W. Bohn^{*,†}

Department of Chemical and Biomolecular Engineering, University of Notre Dame, Notre Dame, Indiana 46556, and Beckman Institute for Advanced Science and Technology, University of Illinois at Urbana–Champaign, 405 North Mathews Avenue, Urbana, Illinois 618101

Received: July 15, 2008; Revised Manuscript Received: October 9, 2008

Ionic transport in nanopores is dependent on the nature of the electrical communication between the pores and the surrounding environment. A particularly useful fluidic device structure uses nanopores in nanocapillary array membranes (NCAMs) as electrically switchable valves between vertically separated microfluidic channels. In the off-state, the gate isolates the fluidic environments in the microchannels, but when the appropriate forward-bias voltage is applied, it selectively allows ions and analytes to move between the microchannels. However, the populations of species in the microfluidic channels are perturbed from their steady-state values due to ion accumulation and depletion effects. Experiments conducted here characterize the electrical conduction along the length of a microfluidic channel, and laser-induced fluorescence probes the formation of a high- and low-concentration regions of fluorescent dye before and after application of forward- and reverse-bias voltage pulses in both small ($a = 10$ nm) and large ($a = 100$ nm) pore NCAMs. In all cases, switching from injection (transport across the NCAM) to microfluidic flow (transport only in the microfluidic channel) results in a multiphasic current recovery profile, signifying the presence of ion accumulation and depletion regions at the microfluidic–nanofluidic boundary, that is, in the region adjacent to the NCAM. The behavior is consistent with a model in which a volume of altered ion concentration is created at the microfluidic–nanofluidic boundary upon injection. Switching back to microfluidic flow causes this altered conductivity region to be swept from the microfluidic channel, re-establishing the steady state conduction properties.

Introduction

The behavior, manipulation, and control of fluids confined in spaces with dimensions, $a \sim 1$ –100 nm, constitutes nanofluidics. Fluids confined in these structures exhibit behaviors not observed in larger structures, because the physical scaling lengths characteristic of the fluid, for example, Debye length, hydrodynamic radius, are comparable in size to the nanostructure itself. Nanocapillary array membranes (NCAMs) are synthetic membranes that contain large areal densities, $N_p \sim 10^8$ cm⁻², of either conical or cylindrical nanopores of high aspect ratio, that is, length-to-diameter ratios, $l/a > 50$. NCAMs have been studied extensively, because they represent especially simple nanofluidic structures that may be used either for model studies of nanofluidic transport or for applications in hybrid microfluidic–nanofluidic architectures. Fundamental transport studies can exploit the large surface-to-volume ratio, providing a pathway to interrogate fluid properties by observing how the fluid behaves when it is exposed to external stimuli, for example, voltage, or confined in a small space, that is, the interior of the nanopore. When incorporated into three-dimensional hybrid devices, NCAMs can isolate and maintain two chemically disparate environments within the same device, perform rapid and efficient mixing,¹ facilitate mass selective transport of analytes,^{2,3} and realize preparative separations of mass-limited samples.^{4,5}

When an NCAM is sandwiched between two oblique microfluidic channels, fluidic isolation or mixing may be ac-

complished by manipulating the pore diameter, a , the surface density, σ , and, thus, the zeta potential, ζ , of the nanopore and the ionic strength of the fluid in contact with the nanopores. For example, a univalent electrolyte with a 1 mM concentration flowing through a 10 nm cylindrical pore with a strong positive surface charge density produces an electrical double layer at the surface of the cylindrical pore whose thickness is defined by the inverse Debye length, κ ,

$$\kappa = \sqrt{\frac{8\pi n e^2}{\epsilon k T}} \quad (1)$$

where n is the ion number density, e is the electron charge, ϵ is the dielectric constant, k is the Boltzman constant, and T is the temperature. The inverse Debye length, in this case, is $\kappa \sim 0.11$ nm⁻¹, which, with $a = 10$ nm, gives $\kappa a \sim 1$. Physically, the electrical double layer spans the pore, and over a very large range of surface charge densities the pore contains a preponderance of counterions. Consequently, co-ions are largely excluded, giving rise to ion permselective behavior. The electrical equilibrium thus established acts to isolate the two chemical environments on either side of the nanopore and has been used to maintain pH⁶ or ionic concentration gradients across a nanopore in the absence of an externally applied electric field.

When an NCAM connects two microfluidic channels, and a potential difference is applied between the channels, ion depletion and accumulation phenomena are observed at the microfluidic–nanofluidic boundary,⁷ a phenomenon observed in other types of ion permselective membranes^{8,9} and known as concentration polarization. These ion reorganization effects result in differential transport¹⁰ of ions through the nanopores

* Author to whom correspondence should be addressed. E-mail: pbohn@nd.edu.

[†] University of Notre Dame.

[‡] University of Illinois at Urbana–Champaign.

and nonlinear electrokinetic phenomena, features that can be exploited to effect sample stacking¹¹ or preconcentrate analytes^{12,13} such as proteins.^{14,15} For example, Chatterjee et al. used compact models to simulate the I - V characteristics of microchannels connected to 30 and 15 nm pore diameter NCAMs.¹⁶ They observed that differential ion transport leads to permselectivity and highlighted the significant role that surface charge density and membrane capacitance play in electrokinetic transport in NCAMs. Pu et al. studied the electrokinetic transport of rhodamine and fluorescein dyes in 60 nm deep nanochannels connected to 100 μm deep microchannels and observed enrichment at the cathode and depletion at the anode of both dyes, despite the fact that they are oppositely charged.¹⁷ This observation was attributed to preferential transport of ions toward the cathode due to the overlap of the electric double layer in the nanochannels. Plecis et al. observed hindered transport by diffusion of charged species in a 50 nm nanoslit.⁷ They attributed the hindered transport to an exclusion-enrichment effect caused by the electrical double layer (EDL) expanding in the nanoslit, thereby decreasing the effective width of the nanoslit. However, the EDLs from opposite walls do not have to overlap for the effect to be observed, and other properties, such as the net charge of the diffusing species and the zeta potential of the surface, were implicated in the hindered diffusion. These studies all highlight the central nature of nanopore charge and its distribution in understanding fundamental characteristics of nanofluidic transport^{18–23} and its use for analysis^{24–27} and separations.^{28–30}

Of special relevance to the work described here is a set of numerical simulations performed by Jin et al. to investigate ion accumulation and depletion mechanisms at microfluidic–nanofluidic boundaries.³¹ These authors studied single 10 nm \times 1 μm (long) slit pores under both positive- and negative-bias conditions to capture the transient phenomena associated with injection–recovery cycles. These studies identified multiphasic current signatures and electrical-mechanical coupling effects, such as induced convective transport at the micro–nano junction. The injection–recovery sequence studied is identical to that used in the present work. Here, we describe a series of experiments targeting the behavior of integrated, NCAM-coupled microfluidic channels during injection–recovery cycles. These cycles are designed specifically to allow the ion populations to be perturbed (during injection), and then the recovery to steady state is studied by monitoring both the microchannel current as well as the evolution of the intensity of a fluorescent marker placed in the source channel.

Experimental Section

Materials. Mono- and dibasic salts of sodium phosphate were used to prepare 10 mM, pH 7.4 phosphate buffer solution. Fluorescein disodium salt (Sigma-Aldrich) was dissolved in 10 mM, pH 7.4 phosphate buffer to make a 5 μM fluorescein solution. Deionized (DI) H_2O from a Mini-Q UV-Plus system (Millipore) was used to prepare all solutions, and all reagents were used as received.

Device Fabrication. The four-terminal device used in these experiments was constructed by sandwiching polycarbonate NCAMs between two crossed polydimethylsiloxane (PDMS) microfluidic channels. The PDMS microfluidic channels, 12 mm in length and 50 μm in height and width, and reservoirs were fabricated using standard rapid prototyping and soft lithography protocols.³² Poly(vinylpyrrolidone)-coated, polycarbonate track-etched membranes (Osmonics) of 100 nm pore diameter ($N_p =$

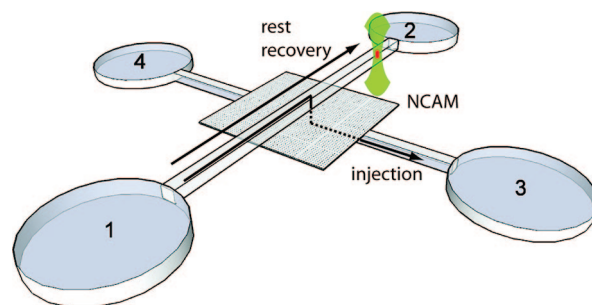


Figure 1. Schematic diagram illustrating the four-terminal NCAM-connected integrated microfluidic architecture. 50 $\mu\text{m} \times 50 \mu\text{m}$ PDMS microchannels cross at 90°, where the NCAM provides electrically switchable fluidic communication between the two. The current measurement paths for the rest and recovery states in source channel, 1-2, and the injection state between source and receiving channels, 1-3, are shown. The relative position of the fluorescence measurements is shown near reservoir 2.

$4 \times 10^8 \text{ cm}^{-2}$), and 10 nm pore diameter ($N_p = 6 \times 10^8 \text{ cm}^2$) with a thickness of $\sim 6 \mu\text{m}$ were used.

Transport Control and Measurement. A schematic of the microchannel architecture used in our study is shown in Figure 1. The microchannel labeled (1,2), filled with a fluorescein dye probe solution, is designated the source channel and that labeled (3,4) the receiving channel. Each microchannel is terminated with a reservoir that holds reserve fluid. The microchannels were vacuum filled and the reservoir heights adjusted to minimize Laplace pressure-induced flow. Platinum wires (250 μm diameter, Goodfellow Corp.) placed in the terminal reservoirs served as bias electrodes. To switch the high voltage power supplies (Bertran High Voltage, 0–3 kV controlled by Labview (National Instruments) software) between the steady state and injection state, a computer controlled 8-relay system controlled by Labview was used. The current in the source channel was continuously monitored during the experiments using an external resistor and nanovoltmeter (Keithley Instruments). At steady state, 40 V was applied to one end of the source channel, while the other end was electrically grounded, and the receiving channel floated. In the $\Delta t = 5 \text{ s}$ injection phase, the entire source channel was biased relative to the receiving channel by holding both terminals of each microchannel at the required potential. During injection, the applied voltage is designated as $\Delta V = V_{\text{receiving}} - V_{\text{source}}$. Current measurements were performed between reservoirs 1 and 2 during steady state and between reservoirs 1 and 3 during injection. Fluid transfer from one microfluidic channel to the other was simultaneously monitored by single spot epi-illumination laser-induced fluorescence (LIF). LIF was used to interrogate the behavior of fluorescein probe in the source channel, in response to the injection–recovery sequences under study.

Results and Discussion

In these experiments, an injection–recovery technique is employed that is capable of providing insight into perturbed ion populations at the nanofluidic–microfluidic boundary and their effect on channel conductance. Typical operation includes three states: rest, injection, and recovery. Initially, the system is in the rest state during which a potential of 40 V is applied along microchannel 1-2, and microchannel 3-4 electrically floats. The injection state then is initiated, during which ions are transferred from one microchannel to the other for 5 s. During the injection stage, the source channel is either positively biased relative to the receiving channel or vice versa. When $\Delta V > 0$,

TABLE 1: Applied Voltages During Rest, Injection, and Recovery

	positive bias				negative bias			
	1	2	3	4	1	2	3	4
rest	40	0	F	F	40	0	F	F
injection	0	0	40	40	40	40	0	0
recovery	40	0	F	F	40	0	F	F

the external electric field is from the receiving channel to the source channel and this is defined as a positively biased case (see Table 1). When $\Delta V < 0$, the external electric field is from the source channel to the receiving channel and this is defined as a negatively biased case. At the end of the injection stage, the applied potentials on the electrodes are reverted back to those of the rest stage, and the system evolves back to steady state. The applied voltages used are summarized in Table 1. Because the current path changes, the current is measured differently in the three states; in rest and recovery states the current is measured in the 1-2 microchannel, while during injection it is measured between the 1-2 microchannel and the 3-4 microchannel, that is, across the NCAM.

The focus of these experiments is understanding how the microchannel conductivity and ion population distributions change during and after injection, by measuring current and the fluorescence of a probe in the source channel adjacent to the membrane. The NCAM pore diameter was changed from 10 to 100 nm, covering the cases $\kappa a \sim 1$ and $\kappa a > 1$, respectively, and both structures were studied using injection potentials $\Delta V = +40$ and -40 V. The current, I , was measured continuously through the injection cycle and is given by

$$I = \frac{\rho A \Delta \varphi}{l} \quad (2)$$

where ρ is the resistivity of the solution, A is the cross-sectional area, l is the length, and $\Delta \varphi$ is the applied potential difference, all measured along the conduction path (different conduction paths used in injection and recovery states).

Case 1: $a = 100$ nm; $\Delta V = +40$ V. Figure 2 shows the relationship of the current and fluorescence to the applied voltage during three successive rest–injection–recovery cycles for $a = 100$ nm, $\Delta V = +40$ V. The current transient shown in the inset of Figure 2 is divided into three regions: a rest state (a), injection state (b), and recovery state (c). After injection, the current initially increases rapidly, at the (b)–(c) boundary, as the current path is re-established in the microfluidic channel. In fact, the current in the microchannel is elevated above its value in the rest state, subsequently recovering to the steady state over ~ 40 s, where it is stable until the next injection event.

In the 100 nm pore NCAM, eq 1 predicts that the Debye layer occupies a small volume, $\sim 3\%$ of the pore diameter, meaning that the bulk of the nanopores is filled with fluid whose chemical composition is that of the bulk fluid in the microchannel. The surfaces of both source and receiving PDMS microchannels are negatively charged, $\zeta_{\text{PDMS}} < 0$, meaning that the counterions are cations. When the receiving channel is biased positive relative to the source channel, the positively charged counterions are driven from the receiving channel to the source channel, creating a net accumulation of counterions at the micro–nano boundary in the source channel. Then, when the system is switched to the recovery phase, the current is monitored in the source channel, and since the conductivity of the electrolyte solution is governed by the relative mobilities of the cations, $\mu \sim 2 \times 10^{-5} \text{ cm}^2 \text{ s}^{-1}$, and anions, $\mu \sim 0.9 \times 10^{-5} \text{ cm}^2 \text{ s}^{-1}$,³¹ the influx of ions into the microchannel produces

a region of higher conductivity in the center of the microchannel. When the recovery phase begins and the current path is switched back to the microchannel, this region of higher conductivity leads to a higher current. Once the recovery voltage is restored, the region of lower resistivity begins to move and experience diffusional broadening as the fluid moves to the reservoir in the source channel, thus removing the high conductivity fluid zone and returning the current to its rest state value.

Laser induced fluorescence (LIF) was used simultaneously to monitor bulk fluid transport of $5 \mu\text{M}$ fluorescein, Fl^{2-} , in 10 mM phosphate buffer at pH 7.4 in the source channel. The laser was focused in the microchannel ~ 1 mm from the intersection, and LIF was used to monitor changes in fluorescence intensity during three successive rest–injection–recovery phases, as shown in Figure 2. When the injection voltage is applied across the NCAM, the fluorescent intensity is initially unchanged; however, ~ 20 s after the injection, a reproducible decrease in intensity is observed which later recovers to the steady-state fluorescent intensity. This transient decrease in intensity is attributed to the transfer of buffer solution from the receiving channel to the source channel, discussed above. Immediately after initiation of the recovery voltage, the volume directly under the NCAM has a decreased $[\text{Fl}^{2-}]$ due to the transfer of buffer from the receiving channel. Once flow commences in the source channel, this volume element starts to move to the reservoir at $\sim 0.5 \text{ mm s}^{-1}$, and the delay observed in the LIF scan directly correlates with the time required for transport from the NCAM to the observation zone. The zone of decreased probe concentration transits the observation zone rapidly, and the fluid behind it has the bulk $[\text{Fl}^{2-}]$, so the fluorescence intensity returns to its original value. Fluorescence microscopy movies (not shown) confirm that the transient decrease is due to a volume element of decreased fluorescein concentration moving through the detection region.

Case 2: $a = 100$ nm; $\Delta V = -40$ V. In a second set of experiments with the same NCAM structure, the voltage polarity was changed to $\Delta V = -40$ V, with the fluorescence and current data obtained over three successive rest–injection–recovery cycles being shown in Figure 3. Both current and fluorescence data are the inverse of that obtained for $\Delta V = +40$ V. The current transient again begins by recovering to a metastable level as current is re-established in the source channel, but now the initial recovery current is below that of the rest state. Then, after ~ 50 s, the current smoothly increases up to the rest state value. This behavior can be understood based on the same physical principles used to discuss the $+40$ V case. Here, however, the direction of cation transport is from the source to receiving channel; thus, the decreased initial source channel current in the recovery phase is associated with the formation of a depletion region in the source channel at the nano–micro boundary. This region, which is localized at the NCAM junction, when the recovery stage begins, exhibits a higher resistivity, causing the overall resistance of the source channel to increase and the current to decrease. The region moves toward the reservoirs in the source channel and broadens via diffusion, eventually exiting the microchannel, at which point the current recovers to the rest state value.

It is worth noting that the $\Delta V = +40$ and -40 V cases are both characterized by a biphasic recovery profile, in which the current returns to a metastable level immediately after re-establishing in the (1,2) source microfluidic channel, before returning to its steady-state value some time later. Similarly, in both cases, the biphasic recovery is attributed to a confined space charge created by differential transport across the NCAM during

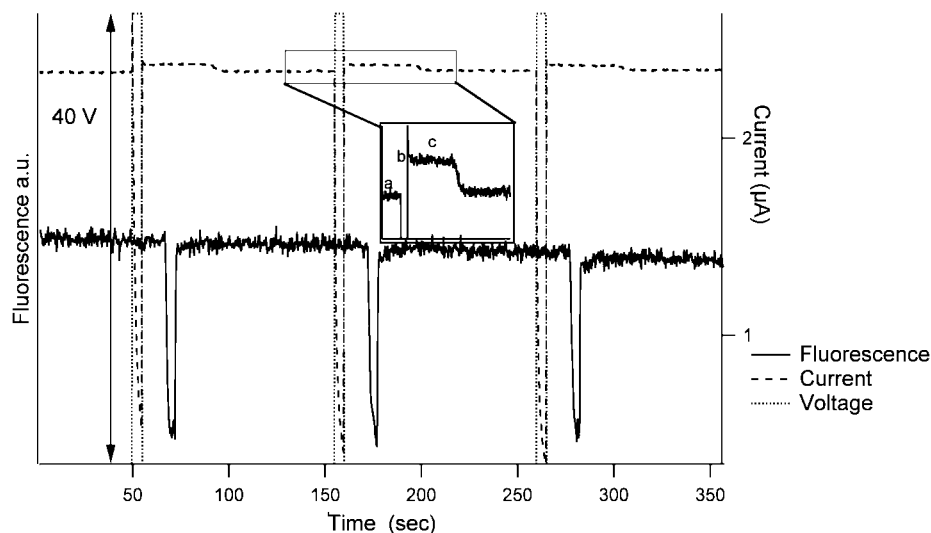


Figure 2. Current and fluorescence measurements during several consecutive rest-injection-recovery cycles in the case of $a = 100$ nm, $\Delta V = +40$ V. (Inset) Magnified portion of the current profile in the rest (a), injection (b), and recovery (c) states during one representative cycle. The voltage trace shows the magnitude of the applied potential across the NCAM only.

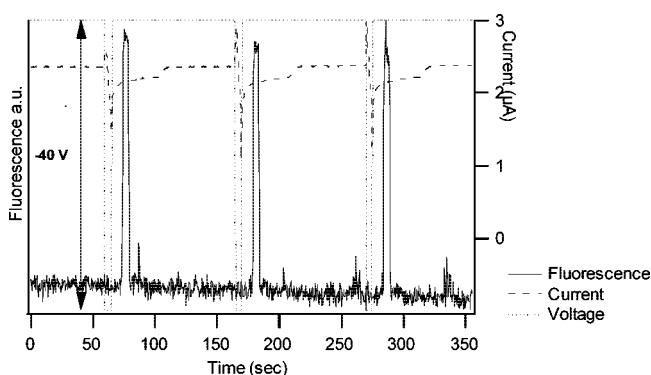


Figure 3. Current and fluorescence measurements during several consecutive rest-injection-recovery cycles in the case of $a = 100$ nm, $\Delta V = -40$ V. The voltage trace shows the magnitude of the applied potential across the NCAM only.

injection. The space charge regions of accumulated and depleted ion densities at $\Delta V = +40$ and -40 V, respectively, in the source channel, then move toward the grounded reservoir once the recovery potential is re-established. Although they certainly broaden by longitudinal diffusion during this phase of the experiment, the current only returns to the rest state value, when the region of altered conductivity is removed from the microchannel.

The fluorescence data similarly bear an inverse relationship to the fluorescence data at $\Delta V = +40$ V. Initially, in the recovery phase, the fluorescence is unchanged, and then a transient increase in fluorescence intensity is observed. This zone of increased fluorescence intensity is a clear sign of sample stacking. The transfer of fluid is determined by the direction of electroosmotic flow in the microchannels, that is, from source to receiver. However, electrophoresis of the Fl^{2-} transports the probe against the direction of electroosmotic flow, which, when coupled to the formation of the space charge region at the NCAM interface in the source channel, results in Fl^{2-} entering the NCAM and moving into the receiving channel more slowly than the cationic buffer components.

Case 3: $a = 10$ nm; $\Delta V = +40$ V. The 10 nm pore diameter NCAMs access the limiting case, $\kappa a \leq 1$, where the opposed double layers overlap and interact. A detailed set of simulations focused on the impact of ion depletion and accumulation on

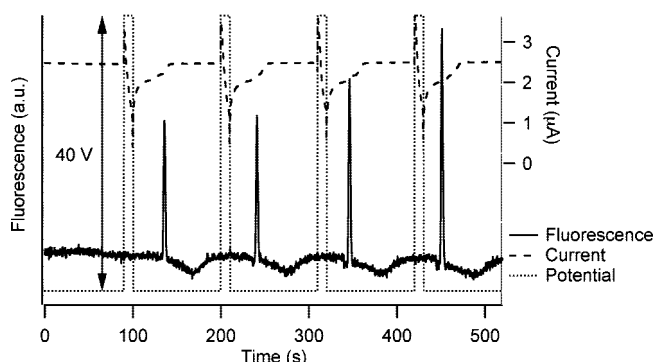


Figure 4. Current and fluorescence measurements during several consecutive rest-injection-recovery in the case of $a = 10$ nm, $\Delta V = +40$ V. The voltage trace shows the magnitude of the applied potential across the NCAM only.

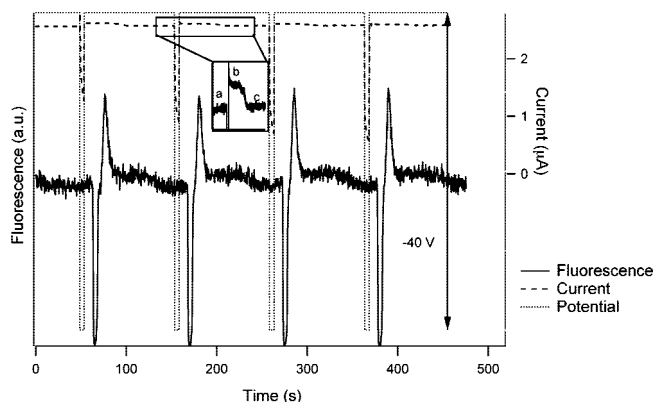


Figure 5. Current and fluorescence measurements during several consecutive rest-injection-recovery cycles in the case of $a = 10$ nm, $\Delta V = -40$ V. (Inset) Magnified portion of the current profile in the rest, injection, and recovery states during one representative cycle. The voltage trace shows the magnitude of the applied potential across the NCAM only.

fluidic transport in a single 10 nm slit pore has been reported by Jin et al.³¹ These calculations provide the context for interpreting the current transients and fluorescence profiles shown in Figures 4 and 5.

The data shown in Figure 4 for $a = 10$ nm, $\Delta V = 4$ V are qualitatively similar to the data shown in Figure 3 for $a = 100$

nm, $\Delta V = -40$ V. This type of reversal of behavior between $\kappa a \gg 1$ and $\kappa a \leq 1$ has been observed for NCAM mediated transport between microchannels since the earliest experiments.³³ Although the data of Figures 3 and 4 are similar, the mechanisms responsible for them are very different and reflect the special nature of transport in nanostructures at the $\kappa a \leq 1$ limit. When the 10 nm NCAM is biased at $\Delta V = +40$ V during the injection phase, both cations and anions deplete in the source channel³¹ (and accumulate in the receiving channel, although that is not probed in these experiments). In particular, Figure 12 of ref 31 shows the direction and magnitude of electrokinetic flow vectors in both channels. Since the NCAM pores are positively charged, and the Debye layer occupies $\sim 60\%$ of the pore diameter, the pores are permselective for anions, and cations are repelled from the pore. Thus, cations, which would enter the NCAM from the receiving side, cannot do so. Furthermore, the flux of cations in the source channel is toward the reservoirs and away from the NCAM, resulting in a reduction in cation concentration at the NCAM. At the same time, the anion flux in the receiving channel is toward the reservoir and away from the NCAM junction, so anion flux entering the NCAM pores cannot compensate for the anions exiting the nanopores on the source side. These effects result in an ion depleted region at the NCAM junction that decreases the conductivity of the bulk solution such that, at the onset of the recovery stage, the current is significantly less than that of the bulk solution as indicated in Figure 4. The current recovers to its original value as the ion depleted region is swept into the reservoir of the microchannel, just as in Case 2. Furthermore, the creation of the space charge region establishes a new field, thereby inducing electroosmotic flow of the second kind.³⁵ Electroosmotic flow of the second kind accentuates mixing at the micro–nano junction, enhancing the delivery of doubly charged fluorescein molecules and raising the local concentration, $[F^{2-}]$.^{9,15,36}

Bulk fluid movement in the device employing a 10 nm NCAM was followed by measuring the fluorescence profile of four injection cycles, as shown in Figure 4. Again, just as for Case 2, a transient increase in fluorescence intensity, indicating a stacked region of probe, is observed. Here, the large difference in mobilities of anions and cations, the permselectivity of the NCAM, and the induced space charge region result in the F^{2-} probe being driven toward the NCAM, but because of the large difference in fluidic capacity between the microchannel and the collective nanochannels the F^{2-} stacks at the NCAM. The difference in capacity can be appreciated by comparing the volume of the microchannel above the NCAM, $V_{\text{micro}} = 50 \mu\text{m} \times 50 \mu\text{m} \times 50 \mu\text{m} = 125 \text{ pL}$, with the total volume represented by the pores in the NCAM, $V_{\text{nano}} = A_{\text{NCAM}} N_p V_{\text{nanopore}} = 7.5 \text{ fL}$, for the NCAMs used in these latter experiments.

Case 4: $a = 10$ nm; $\Delta V = -40$ V. Next, the direction of the applied potential bias was reversed by biasing the source channel at $+40$ V relative to the receiving channel at ground. Figure 5 shows that the current data are qualitatively similar to Case 1 ($\kappa a \gg 1$, opposite polarity), suggesting the formation of an accumulation region in the source channel, using the same reasoning used to establish the formation of the depletion region in the source channel in Case 3. Since there is a net increase of ion density in the source channel, a volume element of increased conductivity and, hence, an increase in the current at the onset of the recovery stage are expected, as is indeed observed. Furthermore, the data shown in Figure 5 (inset) indicate that the current later recovers to its steady state in the characteristic biphasic manner, as the region of ion accumulation is swept to the reservoirs of the source channel.

The fluorescence data in Figure 5 are significantly more complicated than the preceding cases, showing a transient characterized by a decrease in intensity, followed immediately by an increase, before returning to steady state. Significantly, the behavior is reproducible and points to juxtaposed regions of depleted and enhanced fluorophore concentration speaking to the complex dynamics which must be driving the probe populations in this case. We are currently working to develop reliable simulation tools to treat a large array of coupled nanopores to help unravel this unexpected behavior.

Conclusions

Conductance and LIF measurements were applied to study the behavior of nanofluidically coupled microfluidic channels using a perturbation approach employing a rest–injection–recovery protocol. Several key features emerge from these investigations. First, the behavior in all cases can be explained by the formation of space charge regions adjacent to the NCAM in both source and receiving microchannels. These space charge regions constitute volumes of enhanced (accumulation) or diminished (depletion) conductivity, so that, immediately after re-establishing current flow in the source channel following injection (recovery phase), the fluid in the microchannel contains a central region of altered conductivity, either raising or lowering the current relative to steady state. Re-establishing microfluidic flow then eventually moves the altered conductivity region out of the microchannel and into the larger volume reservoir where its influence on conduction is diluted to negligible levels. These events lead to a natural, biphasic current signature in the recovery phase, which is reproducible across different cycles and which, because it is observed under all limiting conditions, would have to be considered a general feature of NCAM-mediated fluidic coupling between microchannels. Furthermore, the 10 nm pore NCAM data agree qualitatively with previously published simulations reported by Jin et al. on single 10 nm pores in which the multiphasic behavior is ascribed to the formation of space charge regions of enhanced or diminished conductivity. Although the experiments are performed with membranes containing arrays of ($> 10^3$) nanopores and the simulations address a single nanopore, the qualitative agreement between simulation and experiment lends credence to the physical interpretation in terms of the formation of space charge regions. The formation of the space charge region is also coupled with altered bulk flow, as assessed through LIF experiments away from the NCAM in the source channel. The fluorophores exhibit either transient increases (sample stacking) or decreases in response to the creation of space charge regions in the source microchannel and the vast difference in volume flow capacity between microchannels and the assembly of nanocapillaries constituting the NCAMs, even for relatively small fluorophores, such as the F^{2-} probe used in the present experiments.

Acknowledgment. This work was supported by the National Science Foundation Center for Advanced Materials for Water Purification with Systems through cooperative agreement CTS 01 20978 and by the Department of Energy through Grant DE FG02 07ER15851.

References and Notes

- (1) Kuo, T. C.; Kim, H. K.; Cannon, D. M.; Shannon, M. A.; Sweedler, J. V.; Bohn, P. W. *Angew. Chem., Int. Ed.* **2004**, *43*, 1862.
- (2) Kuo, T. C.; Cannon, D. M.; Chen, Y. N.; Tulock, J. J.; Shannon, M. A.; Sweedler, J. V.; Bohn, P. W. *Anal. Chem.* **2003**, *75*, 1861.
- (3) Kuo, T. C.; Cannon, D. M.; Shannon, M. A.; Bohn, P. W.; Sweedler, J. V. *Sens. Actuators, A* **2003**, *102*, 223.

- (4) Iannaccone, J. M.; Jakubowski, J. A.; Bohn, P. W.; Sweedler, J. V. *Electrophoresis* **2005**, *26*, 4684.
- (5) Wernette, D. P.; Swearingen, C. B.; Cropek, D. M.; Y, L.; Sweedler, J. V.; Bohn, P. W. *Analyst* **2006**, *131*, 41.
- (6) Fa, K.; Tulock, J. J.; Sweedler, J. V.; Bohn, P. W. *J. Am. Chem. Soc.* **2005**, *127*, 13928.
- (7) Plecis, A.; Schoch, R. B.; Renaud, P. *Nano Lett.* **2005**, *5*, 1147.
- (8) Leinweber, F. C.; Tallarek, U. *Langmuir* **2004**, *20*, 11637.
- (9) Leinweber, F. C.; Tallarek, U. *J. Phys. Chem. B* **2005**, *109*, 21481.
- (10) Jirage, K. B.; Martin, C. R. *Trends Biotechnol.* **1999**, *17*, 197.
- (11) Zhang, Y.; Timperman, A. T. *Analyst* **2003**, *128*, 537.
- (12) Kovarik, M. L.; Jacobson, S. C. *Anal. Chem.* **2008**, *80*, 657.
- (13) Kovarik, M. L.; Jacobson, S. C. *Anal. Chem.* **2007**, *79*, 1655.
- (14) Wang, Y. C.; Han, J. Y. *Lab Chip* **2008**, *8*, 392.
- (15) Wang, Y. C.; Stevens, A. L.; Han, J. Y. *Anal. Chem.* **2005**, *77*, 4293.
- (16) Chatterjee, A. N.; Cannon, D. M.; Gatimu, E. N.; Sweedler, J. V.; Aluru, N. R.; Bohn, P. W. *J. Nanopart. Res.* **2005**, *7*, 507.
- (17) Pu, Q. S.; Yun, J. S.; Temkin, H.; Liu, S. R. *Nano Lett.* **2004**, *4*, 1099.
- (18) Hug, T. S.; de Rooij, N. F.; Staufer, U. *Microfluid. Nanofluid.* **2006**, *2*, 117.
- (19) Karnik, R.; Castelino, K.; Majumdar, A. *Appl. Phys. Lett.* **2006**, *88*, 123114.
- (20) Schoch, R. B.; Renaud, P. *Appl. Phys. Lett.* **2005**, *86*, 253111.
- (21) Schoch, R. B.; van Lintel, H.; Renaud, P. *Phys. Fluids* **2005**, *17*, 100604.
- (22) Tessier, F.; Slater, G. W. *Electrophoresis* **2006**, *27*, 686.
- (23) Yaroshchuk, A.; Zhukova, O.; Ulbricht, M.; Ribitsch, V. *Langmuir* **2005**, *21*, 6872.
- (24) Mannion, J. T.; Craighead, H. *Biopolymers* **2006**, *85*, 131.
- (25) Melechko, A. V.; McKnight, T. E.; Guillorn, M. A.; Merkulov, V. I.; Ilic, B.; Doktycz, M. J.; Lowndes, D. H.; Simpson, M. L. *Appl. Phys. Lett.* **2003**, *82*, 976.
- (26) Reisner, W.; Morton, K. J.; Riehn, R.; Wang, Y. M.; Yu, Z. N.; Rosen, M.; Sturm, J. C.; Chou, S. Y.; Frey, E.; Austin, R. H. *Phys. Rev. Lett.* **2005**, *94*, 196101.
- (27) Wolfrum, B.; Zevenbergen, M.; Lemay, S. *Anal. Chem.* **2008**, *80*, 972.
- (28) Garcia, A. L.; Ista, L. K.; Petsev, D. N.; O'Brien, M. J.; Bisong, P.; Mammoli, A. A.; Brueck, S. R. J.; Lopez, G. P. *Lab Chip* **2005**, *5*, 1271.
- (29) Tegenfeldt, J. O.; Prinz, C.; Cao, H.; Huang, R. L.; Austin, R. H.; Chou, S. Y.; Cox, E. C.; Sturm, J. C. *Anal. Bioanal. Chem.* **2004**, *378*, 1678.
- (30) Wang, K. G.; Yue, S. L.; Wang, L.; Jin, A. Z.; Gu, C. Z.; Wang, P. Y.; Feng, Y. C.; Wang, Y. C.; Niu, H. B. *Microfluid. Nanofluid.* **2006**, *2*, 85.
- (31) Jin, X. Z.; Joseph, S.; Gatimu, E. N.; Bohn, P. W.; Aluru, N. R. *Langmuir* **2007**, *23*, 13209.
- (32) Duffy, D. C.; McDonald, J. C.; Schueller, O.; Whitesides, G. *Anal. Chem.* **1998**, *70*, 4974.
- (33) Kemery, P. J.; Steehler, J. K.; Bohn, P. W. *Langmuir* **1998**, *14*, 2884.
- (34) Jin, X.; Joseph, S.; Gatimu, E. N.; Bohn, P. W.; Aluru, N. *Langmuir* **2007**, *23*, 13209.
- (35) Mishchuk, N.; Gonzalez-Gaballero, F.; Takhistov, P. *Colloids Surf., A* **2001**, *181*, 131.
- (36) Tallarek, U.; Leinweber, F. C.; Nischang, I. *Electrophoresis* **2005**, *26*, 391.

JP806257D